

Coupling vibration analysis of turbine shared support rotor-bearing system with squeeze film dampers

Jiaqi Han

Nanjing University of Aeronautics and Astronautics

Guihuo Luo

Nanjing University of Aeronautics and Astronautics

Fei Wang

Nanchang Hangkong University

Wei Chen (✉ chenwei@nuaa.edu.cn)

Nanjing University of Aeronautics and Astronautics

Lulu Liu

Nanjing University of Aeronautics and Astronautics

Zhenhua Zhao

Nanjing University of Aeronautics and Astronautics

Gang Luo

Nanjing University of Aeronautics and Astronautics

Research Article

Keywords: Turbine shared support structure, Coupling vibration, Squeeze film damper, Rotor-bearing test, Finite-element method

Posted Date: July 6th, 2021

DOI: <https://doi.org/10.21203/rs.3.rs-157225/v1>

License: © ⓘ This work is licensed under a Creative Commons Attribution 4.0 International License.

[Read Full License](#)

Version of Record: A version of this preprint was published at International Journal of Aerospace Engineering on February 5th, 2022. See the published version at <https://doi.org/10.1155/2022/8425735>.

Coupling vibration analysis of turbine shared support rotor-bearing system with squeeze film dampers

Jiaqi Han · Guihuo Luo · Fei Wang · Wei Chen · Lulu Liu · Zhenhua Zhao ·
Gang Luo

J. Han · G. Luo · W. Chen (✉) · L. Liu

Key Laboratory of Aero-Engine Thermal Environment and Structure, Ministry of Industry and Information Technology, College of Energy and Power Engineering, Nanjing University of Aeronautics and Astronautics, Nanjing 210016, China

e-mail: chenwei@nuaa.edu.cn

F. Wang

School of Aircraft Engineering, Nanchang Hangkong University, Nanchang 330063, China

Z. Zhao · G. Luo

State Key Laboratory of Mechanics and Control of Mechanical Structures, Nanjing University of Aeronautics and Astronautics, Nanjing 210016, China

Abstract The turbine shared support structure is used widely in aeroengines, but theoretical and experimental research on a rotor-bearing system containing a shared turbine support structure is lacking. This paper reports research into the coupling vibration response of a squeeze-film-damper rotor-bearing system that has two spools with different rotation speeds and is supported by a turbine shared support structure. The problem is addressed by means of rotor-bearing system tests and the finite-element method. Based on the features of a turboshaft engine with a turbine shared support structure, a rotor-bearing test system with a shared support structure is designed, and a dynamic model of the test system is built based on Timoshenko beam elements. The experimental and simulation results indicate that the unbalanced response of the rotor-bearing system with a shared support structure may involve either the sum or difference of the fundamental frequencies of the rotors of the gas generator and power turbine. The simulations show that the imbalance of the power turbine rotor, the radial and bending stiffnesses of the shared support structure, and the radial clearances of squeeze film dampers at the rear of the rotor-bearing system all affect the coupling response. The amplitude of the coupling response can be suppressed effectively by (i) selecting reasonable parameter values for the turbine shared support structure and (ii) exerting strict control over the spool imbalance.

Keywords Turbine shared support structure · Coupling vibration · Squeeze film damper · Rotor-bearing test · Finite-element method

1 Introduction

The core components of an aeroengine are its rotor-bearing systems, and the vibration characteristics of the latter determine directly whether the engine can work in harsh environments with high temperatures, pressures, speeds, and high loads, meanwhile, the vibration condition which has a critical influence on the overall performance of the engine. With improvements in aeroengine performance and increased reliability requirements, modern aeroengine rotor-bearing systems are mostly dual-rotor ones. The support scheme at the turbine involves rotor-bearing systems with either intermediate bearings or a turbine shared support structure (SSS), and the different supporting structures result in different coupling vibrations between the rotor-bearing systems.

Of the two support schemes, the turbine SSS is effective in large turbofan engines at coordinating the larger transition ducts between the high-pressure and low-pressure turbines, such as in the GE90 and CF6-50 aeroengines, and it has a better impact on the clearances of high-pressure-ratio components in the hot section of mid-size turbofan engines compared to when intermediate bearing support is used [1,2]. The SSS is also effective at controlling the power turbine (PT) tip clearance in turboshaft engines and improving the turbine efficiency and maintenance performance. The PT can be replaced without exposing the rear bearing cavity, such as in the MTR390 aeroengine.

In summary, the turbine SSS is used widely in large, medium, and small engines. However, it contains nonlinear components in the form of squeeze film dampers (SFDs), and it carries two spools that rotate simultaneously with different speeds. Therefore, the nonlinear characteristics of the oil films in the SFDs and the mutual vibration between the two spools have adverse effects on the dynamic responses of the rotor-bearing systems in aeroengines.

In the past few decades, much work has been done on coupling vibration analysis of rotor-bearing and whole-engine systems in aeroengines, resulting in many achievements. However, that literature concerns mainly the coupling vibrations of rotor-bearing and whole-engine systems containing intermediate bearings, with the main modeling approaches involving Newton's second law, the Lagrange equations,

and the finite-element (FE) method. Lu et al. [3,4], Thiery and Aidanpää [5], and Yang et al. [6] used Newton's second law to establish an analysis model of a rotor-bearing system containing nonlinear components. Gao et al. [7,8] and Hou et al. [9] used the Lagrange equations to establish a dynamic analysis model of a dual-rotor-bearing system with nonlinear elements and studied its response. Lu et al. [10], Wang et al. [11], Chen [12], Yu et al. [13], and Yang et al. [14] established a dynamic analysis model of dual-rotor-bearing and whole-engine systems using the FE method.

As suggested by the aforementioned studies, Newton's second law and the Lagrange equations tend to be used to establish dynamic analysis models of rotor-bearing systems with simple structures and relatively few degrees of freedom, whereas the FE method tends to be used to establish dynamic analysis models of complex rotor-bearing and whole-engine systems. Therefore, for the present study, we chose the FE method based on Timoshenko beam elements as the modeling method to establish the dynamic analysis model of the test system with a turbine SSS.

Using beam elements to simulate the rotating shaft when establishing an analysis model of a rotor-bearing system of an aeroengine dates back to the 1970s [15–17]; the shaft was simulated as a Timoshenko beam, the dynamic analysis model of the dual-rotor-bearing system containing intermediate bearings was built by component mode synthesis, and the influence of modal truncation on the calculation results was studied. Subsequently, Nelson et al. [18] established a dynamic analysis model of a rotor-bearing system containing SFDs and intermediate bearings and calculated the unbalanced response, the transient response of the blade loss, and the transient response after rotor and stator friction; the calculation results were validated through cross-comparison with other independent documents. Chiang et al. [19,20] established a dynamic analysis model of a rotor-bearing system with intermediate bearings; they calculated the critical speeds and vibration modes of the system and verified them with a single-rotor test system, but the established analysis model did not consider nonlinear factors. Wang et al. [21] established a rotor-bearing model that considered intermediate bearings and nonlinear SFD characteristics, and they carried out a rotor-bearing test to verify their proposed modeling and analysis methods; their research results indicated that it is feasible to build a complex dual-rotor-bearing system with SFDs and bearings using Timoshenko beam elements. The FE modeling method using Timoshenko beam elements has now developed into an effective

method for establishing dynamic analysis models of complex rotor-bearing and whole-engine systems in aeroengines with nonlinear characteristics.

Meanwhile, SFDs are used extensively for vibration suppression in aeroengines [22–25]. However, the severe nonlinear characteristics of the oil-film force in an SFD may result in a dramatic change in the rotor response; more seriously, they may cause instability and damage to the rotor system [26–28]. Many scholars remain concerned about SFD–rotor coupling vibrations. Inayat-Hussain et al. [29] used numerical simulation to investigate the unbalanced response of a single-rotor system containing SFDs without centering springs; with changing shaft imbalance, the response of the rotor system experienced a series of period-doubling bifurcations that caused the system to enter a state of chaotic motion after a period of time, which introduced cyclic stresses and may have rapidly reduced the fatigue limit of the shaft. Qin et al. [30] suggested that the support stiffness has considerable influence on the SFDs; excessive support stiffness causes oil whirl and leads to SFD failure. Chen et al. [31] studied the coupling relationship between rigid-body translation and precession of SFD-unsymmetrical rotor-bearing systems; the results showed that the bifurcation phenomena of asymmetric and symmetric systems are similar, but for asymmetric systems, the stiffness ratio of the left and right supports may destroy the stability of the rotor and cause jumps. Luo et al. [32] studied the nonlinear vibration of a single rotor-bearing system containing SFDs, analyzed the bifurcation phenomenon at different points on the rotor, and compared the dynamic response at different positions; their results showed that the nonlinear force at the support caused both the vibration response and the bifurcations of the spool at different parts to differ.

The aforementioned studies have shown that the presence of SFDs greatly influences the dynamic responses of engine rotor-bearing systems. Choosing inappropriate SFD parameter values may (i) prevent the vibration response of the shaft from being reduced and (ii) degrade the response of the rotor-bearing system. Summarizing the research to date, theoretical and experimental research on rotor-bearing systems with a turbine SSS remains lacking, and SFDs should be considered when establishing dynamic analysis models of complex rotor-bearing systems. Therefore, it is essential to subject turbine-SSS rotor-bearing systems with SFDs to both modeling and coupling-vibration-response research.

The present paper reports on an FE model of a rotor-bearing system with a turbine SSS and containing SFDs. The nonlinear forces exerted by the SFDs are

considered, and the dynamic response of the rotor-bearing system is obtained based on the dynamic model and verified based on test results. The nonlinear dynamic response of the rotor-bearing system with a turbine SSS and SFDs is established based on the verified analysis model.

2 Rotor-bearing system model with shared support structure

2.1 Structure of turboshaft engine

A practical turboshaft engine with a turbine SSS is shown in Fig. 1. The gas generator (GG) rotor uses the 1-0-1 support scheme with two bearings, namely bearings 3 and 4, each of which contains an SFD. The PT shaft has four bearings: bearings 1 and 2 are front bearings, bearings 5 and 6 are rear bearings, and bearings 2 and 6 contain SFDs. The turbine SSS supports the rear three bearings of the two rotors simultaneously.

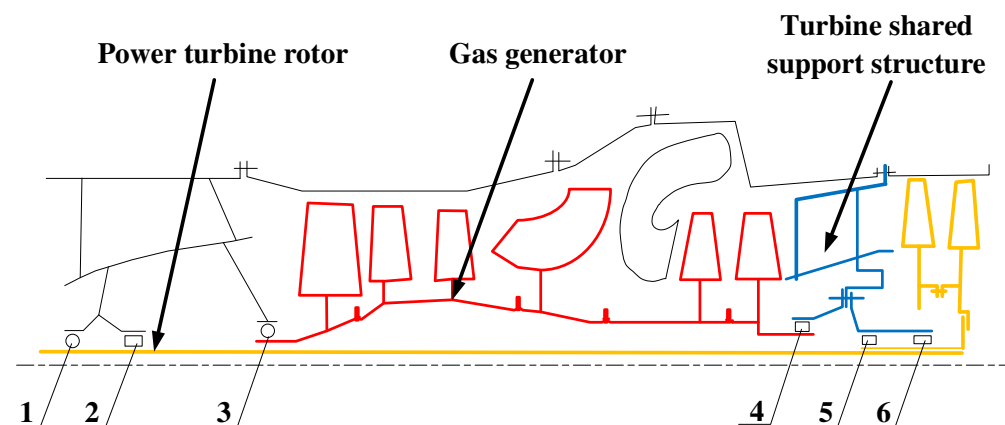
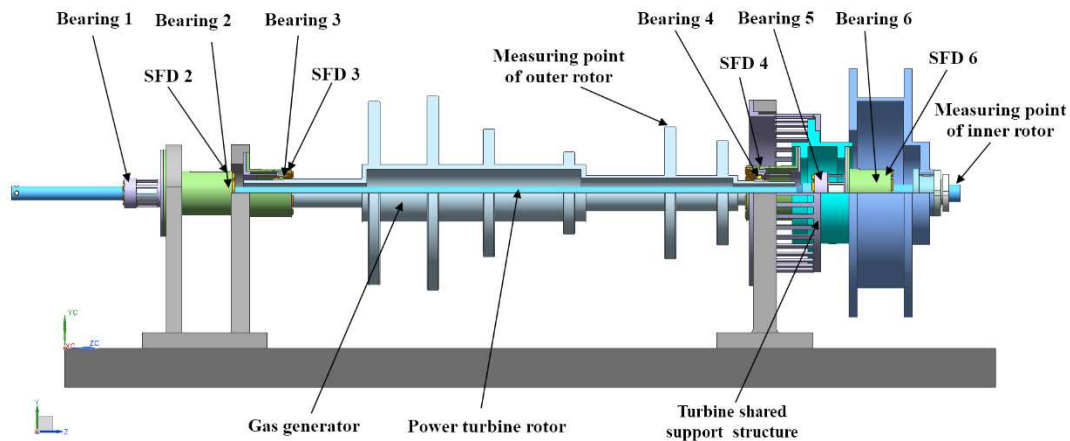


Fig. 1 Structural diagram of turboshaft engine structure

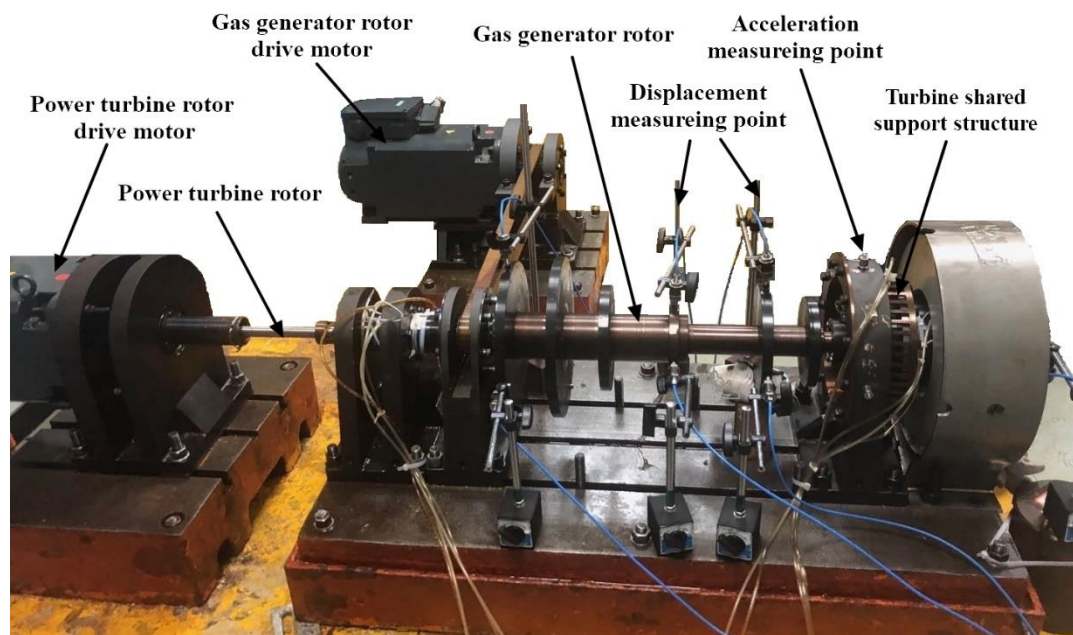
2.2 Structure of test rig

Based on the features of the turboshaft engine with a turbine SSS, we designed the test system containing a turbine SSS as shown in Fig. 2; Fig. 2a shows it schematically, and Fig. 2b shows it photographically. The test system contains two concentric rotating shafts that are connected by a turbine SSS. Each rotating shaft is driven by its own motor so that the two spools can have different working speeds. Bearings 1 and 3 are deep-groove ball bearings that are the axial positioning fulcrums of the PT and GG shafts, respectively, and the other four bearings are all roller bearings; we use the squirrel-cage-rolling-bearing support scheme for supports 1 and 5 and the squirrel-cage-rolling-bearing-SFD support scheme for the rest. In total, we

use eight displacement sensors and two acceleration sensors to monitor the acceleration response of the test system at five axial positions. At a given axial point, one sensor is oriented in the horizontal direction of the rotor-bearing test system and the other is oriented in the vertical direction.



(a)



(b)

Fig. 2 Rotor-bearing test system: (a) schematic; (b) photograph

3 Dynamic model of rotor-bearing system

3.1 Finite-element formulation

Herein, the GG and PT shafts and the SSS are simulated by Timoshenko beam

elements. Only the radial shaft vibrations are considered; the axial and torsional ones are ignored. The degrees of freedom of a shaft section are expressed as

$$\mathbf{q}_e = [u_{e1} \quad v_{e1} \quad \theta_{e1} \quad \varphi_{e1} \quad u_{e2} \quad v_{e2} \quad \theta_{e2} \quad \varphi_{e2}]^T. \quad (1)$$

The mass matrix \mathbf{m}_e , stiffness matrix \mathbf{k}_e , and gyroscope matrix \mathbf{g}_e of the shaft segment are given in Eqs. (2)–(5), the derivations of which are given elsewhere [21]:

$$\mathbf{m}_e = \frac{\rho_e A_e l_e}{840(l_e^2 + 12g)^2} \begin{bmatrix} m_1 & 0 & 0 & m_2 & m_3 & 0 & 0 & m_4 \\ 0 & m_1 & -m_2 & 0 & 0 & m_3 & -m_4 & 0 \\ 0 & -m_2 & m_3 & 0 & 0 & m_4 & m_6 & 0 \\ m_2 & 0 & 0 & m_5 & -m_4 & 0 & 0 & m_6 \\ m_3 & 0 & 0 & -m_4 & m_1 & 0 & 0 & -m_2 \\ 0 & m_3 & m_4 & 0 & 0 & m_1 & m_2 & 0 \\ 0 & -m_4 & m_6 & 0 & 0 & m_2 & m_5 & 0 \\ m_4 & 0 & 0 & m_6 & -m_2 & 0 & 0 & m_5 \end{bmatrix} + \frac{\rho_e I_e}{30(l_e^2 + 12g)^2} \begin{bmatrix} m_7 & 0 & 0 & m_8 & -m_7 & 0 & 0 & m_8 \\ 0 & m_7 & -m_8 & 0 & 0 & -m_7 & -m_8 & 0 \\ 0 & -m_8 & m_9 & 0 & 0 & m_8 & m_{10} & 0 \\ m_8 & 0 & 0 & m_9 & -m_8 & 0 & 0 & m_{10} \\ -m_7 & 0 & 0 & -m_8 & m_7 & 0 & 0 & -m_8 \\ 0 & -m_7 & m_8 & 0 & 0 & m_7 & m_8 & 0 \\ 0 & -m_8 & m_{10} & 0 & 0 & m_8 & m_9 & 0 \\ m_8 & 0 & 0 & m_{10} & -m_8 & 0 & 0 & m_9 \end{bmatrix}, \quad (2)$$

where ρ_e , A_e , and l_e are the material density, cross-sectional area, and axial length of the shaft section, respectively, and we write m_1 – m_{10} as

$$\begin{cases} m_1 = 312l_e^4 + 7056gl_e^2 + 40320g^2 & m_6 = -(6l_e^4 + 168gl_e^2 + 1008g^2)l_e^2 \\ m_2 = (44l_e^4 + 924gl_e^2 + 5040g^2)l_e & m_7 = 36l_e^3 \\ m_3 = 108l_e^4 + 3024gl_e^2 + 20160g^2 & m_8 = (3l_e^2 - 180g)l_e^2 \\ m_4 = -(26l_e^4 + 756gl_e^2 + 5040g^2)l_e & m_9 = (4l_e^4 + 60gl_e^2 + 1440g^2)l_e \\ m_5 = (8l_e^4 + 168gl_e^2 + 1008g^2)l_e^2 & m_{10} = (-l_e^4 - 60gl_e^2 + 720g^2)l_e \end{cases}; \quad (3)$$

$$\mathbf{k}_e = \frac{E_e I_e}{l_e(l_e^2 + 12g)} \begin{bmatrix} b_1 & 0 & 0 & b_2 & -b_1 & 0 & 0 & b_2 \\ 0 & b_1 & -b_2 & 0 & 0 & -b_1 & -b_2 & 0 \\ 0 & -b_2 & b_3 & 0 & 0 & b_2 & b_4 & 0 \\ b_2 & 0 & 0 & b_3 & -b_2 & 0 & 0 & b_4 \\ -b_1 & 0 & 0 & -b_2 & b_1 & 0 & 0 & -b_2 \\ 0 & -b_1 & b_2 & 0 & 0 & b_1 & b_2 & 0 \\ 0 & -b_2 & b_4 & 0 & 0 & b_2 & b_3 & 0 \\ b_2 & 0 & 0 & b_4 & -b_2 & 0 & 0 & b_3 \end{bmatrix}, \quad (4)$$

where E_e is the modulus of elasticity and b_1 – b_4 are formulated as

$$b_1 = 12, b_2 = 6l_e, b_3 = 4l_e^2 + 12g, \text{ and } b_4 = 2l_e^2 - 12g;$$

$$\mathbf{g}_e = \frac{\rho_e I_e}{15(l_e^2 + 12g)^2} \begin{bmatrix} 0 & g_1 & -g_2 & 0 & 0 & -g_1 & -g_2 & 0 \\ -g_1 & 0 & 0 & -g_2 & g_1 & 0 & 0 & -g_2 \\ g_2 & 0 & 0 & g_3 & -g_2 & 0 & 0 & g_4 \\ 0 & g_2 & -g_3 & 0 & 0 & -g_2 & -g_4 & 0 \\ 0 & -g_1 & g_2 & 0 & 0 & g_1 & g_2 & 0 \\ g_1 & 0 & 0 & g_2 & -g_1 & 0 & 0 & g_2 \\ g_2 & 0 & 0 & g_4 & -g_2 & 0 & 0 & g_3 \\ 0 & g_2 & -g_4 & 0 & 0 & -g_2 & -g_3 & 0 \end{bmatrix}. \quad (5)$$

All disk is simulated as a concentrated mass unit that accounts for the gyroscopic effect. The mass matrix \mathbf{m}_e^d and gyroscope matrix \mathbf{g}_e^d of the disk are expressed as

$$\mathbf{m}_e^d = \begin{bmatrix} m_d & 0 & 0 & 0 \\ 0 & m_d & 0 & 0 \\ 0 & 0 & I_d & 0 \\ 0 & 0 & 0 & I_d \end{bmatrix}, \quad (6)$$

$$\mathbf{g}_e^d = \begin{bmatrix} 0 & 0 & 0 & 0 \\ 0 & 0 & 0 & 0 \\ 0 & 0 & 0 & -I_p \\ 0 & 0 & -I_p & 0 \end{bmatrix}, \quad (7)$$

where m_d , I_d , and I_p are the mass, diametral moment, and polar moment of inertia of the disk, respectively.

3.2 Equations of motion for rotor-bearing system

The nonlinear dynamic equations of a rotor-bearing system can be expressed as

$$\mathbf{M}\ddot{\mathbf{u}} + (\mathbf{C} + \boldsymbol{\Omega}\mathbf{G})\dot{\mathbf{u}} + \mathbf{K}\mathbf{u} = \mathbf{F}^e + \mathbf{F}^f, \quad (8)$$

where \mathbf{M} , \mathbf{C} , \mathbf{G} , and \mathbf{K} are the mass, damping, gyroscope, and stiffness matrices of the rotor-bearing system, respectively, which can be obtained according to the method in Sect. 3.1. Here, \mathbf{u} is the displacement vector of the rotor-bearing system, \mathbf{F}^e is the unbalanced force, and \mathbf{F}^f is the nonlinear force introduced by an SFD. The unbalanced force \mathbf{F}^e is expressed as

$$\mathbf{F}^e = \begin{cases} m e \omega^2 \sin(\omega t + \varphi_0) \\ m e \omega^2 \cos(\omega t + \varphi_0) \end{cases}, \quad (9)$$

where m is the unbalanced mass, e is its eccentricity, φ_0 is its initial phase, and ω is the angular velocity of the spool.

Based on the assumptions and boundary conditions in reference [33], we write the nonlinear force introduced by an SFD as

$$\begin{cases} f_x^s = -\frac{\mu_s RL^3}{c^2 \sqrt{(x^2 + y^2)}} [x(\dot{\epsilon}I_2 + \epsilon\dot{\psi}I_1) - y(\dot{\epsilon}I_1 + \epsilon\dot{\psi}I_3)] \\ f_y^s = -\frac{\mu_s RL^3}{c^2 \sqrt{(x^2 + y^2)}} [y(\dot{\epsilon}I_2 + \epsilon\dot{\psi}I_1) + x(\dot{\epsilon}I_1 + \epsilon\dot{\psi}I_3)] \end{cases}, \quad (10)$$

$$\epsilon = \sqrt{x^2 + y^2} / c, \quad (11)$$

$$\dot{\epsilon} = (x\dot{x} + y\dot{y}) / (c\sqrt{x^2 + y^2}), \quad (12)$$

$$\dot{\psi} = (y\dot{x} - x\dot{y}) / (x^2 + y^2), \quad (13)$$

$$\tan \psi = y / x, \quad (14)$$

where x and y are the horizontal and vertical displacements, respectively, of the shaft diameter, L is the axial width of the SFD, R is the average radius of the SFD, c is the SFD radius clearance, μ is the dynamic viscosity of the oil, and I_1 , I_2 , and I_3 are Sommerfeld integrals.

Herein, we treat the squirrel cage as an isotropic linear spring whose stiffness is set directly, and we ignore the stiffness and damping of the rolling bearings. Having established the dynamic analysis model of the rotor-bearing system, we use the implicit Newmark- β method to solve for its response.

3.3 Finite-element model

The analysis model of the test system is shown schematically in Fig. 3, and the structural parameter values for the shaft, disk, squirrel cage, and SFD are given in Tables 1–4, respectively. In Table 3, supports 1–6 are shaft supports with only their radial stiffness (k_{xx} , k_{yy}) considered. Support 7 is the support of the turbine SSS, with both radial stiffness (k_{xx} , k_{yy}) and bending stiffness (k_{xz} , k_{yz}) considered. In the model established herein, we suppose that $k_{xx} = k_{yy}$ and $k_{xz} = k_{yz}$.

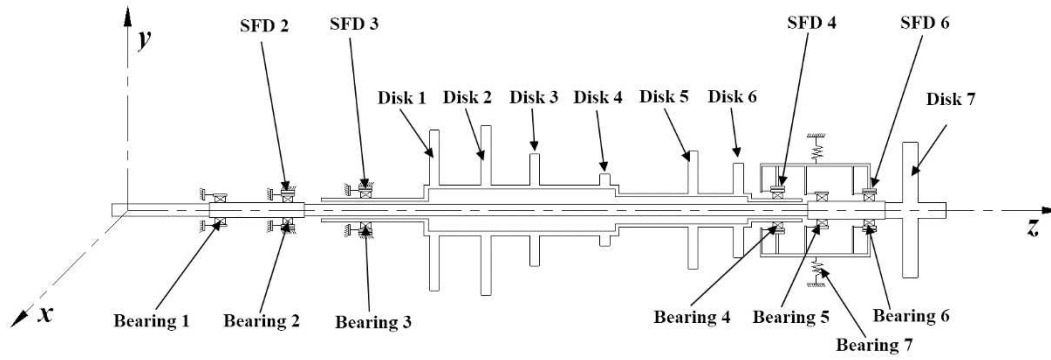


Fig. 3 Finite-element model

Table 1 Parameters of shafts

	Shaft number	Start point [mm]	End point [mm]	Outer diameter [mm]	Inner diameter [mm]
Gas-generator rotor	1	299	451.5	26	37
	2	451.5	740	62	74
	3	740	936	40	46
	4	936	1010	26	37
Power-turbine rotor	5	0	136	0	18.4
	6	136	287.17	0	20
	7	287.17	1013.63	0	16
	8	1013.63	1133.93	0	25
	9	1133.93	1223.63	0	23
Shared support structure	10	947.5	1134.5	120.5	125.5

Table 2 Parameters of disks

	Disk number	Location [mm]	Mass [kg]	IP [$\text{kg}\cdot\text{m}^2$]	Unbalance [$\text{g}\cdot\text{cm}$]	Initial phase
Gas-generator rotor	1	467	4.66	0.03589	2	0
	2	543	5.26	0.04488	2	135
	3	615	2.01	0.00825	1	90
	4	718.5	0.53	0.00111	0	0
	5	849	2.49	0.009724	2	45

	6	916.5	1.48	0.003764	2	0
Power-turbine	7	1164	5.16	0.07261	5	0
rotor						

Table 3 Stiffness of squirrel cages

Bearing number	k_{xx} [N/m]	k_{xz} [N/m]
1	3.77e6	0
2	2.35e5	0
3	1.13e6	0
4	7.1e5	0
5	4.13e6	0
6	2.3e5	0
7	1e8	1e8

Table 4 Parameters of SFD

	Support number	L	R	c	Dynamic viscosity [10^{-2} Pa·s]
Power-turbine	2	19	23	0.05	1.0752
rotor	6	15.5	26.5	0.05	
Gas-generator	3	9.5	25.5	0.05	
rotor	4	17	26.5	0.05	

3.4 Analysis of unbalanced response

Based on the rotor-bearing test system in Sect. 2.2 and the FE model established in Sect. 3.3, we obtain the unbalanced response of the test system by rotor-bearing tests and simulation analysis. We compare the responses obtained by the two methods, thereby verifying the accuracy of the dynamic analysis model established by the FE method. Because the regular response patterns in the horizontal and vertical directions are the same, without loss of generality we take the horizontal response as the example for comparative analysis. Figure 4 shows the horizontal-direction test results obtained from the measuring points on the GG and PT rotors, and Fig. 5 shows the horizontal responses obtained by the FE method from the measuring points on the rotor-bearing system. In Figs. 4 and 5, ω_1 and ω_2 are the fundamental frequencies of the GG and PT spools, respectively.

For safety reasons, the dual-rotor speeds in the tests were increased in two steps: in step 1, the GG spool speed was increased from zero to 6000 rpm while the PT spool remained stationary; in step 2, the GG spool speed remained at 6000 rpm while the PT spool speed was increased from zero to 6000 rpm. In the theoretical analysis, to avoid encountering harmonics such as multiples of 0.5, 1.5, or 2, we set the GG rotor speed to be 1.3 times the PT one.

In both the tests and the FE analysis, the results show that the turbine-SSS rotor system with SFDs has coupling frequency components of $\omega_1 - \omega_2$ and $\omega_1 + \omega_2$, and the results are consistent. Comparing the test and analysis results verifies the accuracy of the analysis model established in Sect. 3.3.

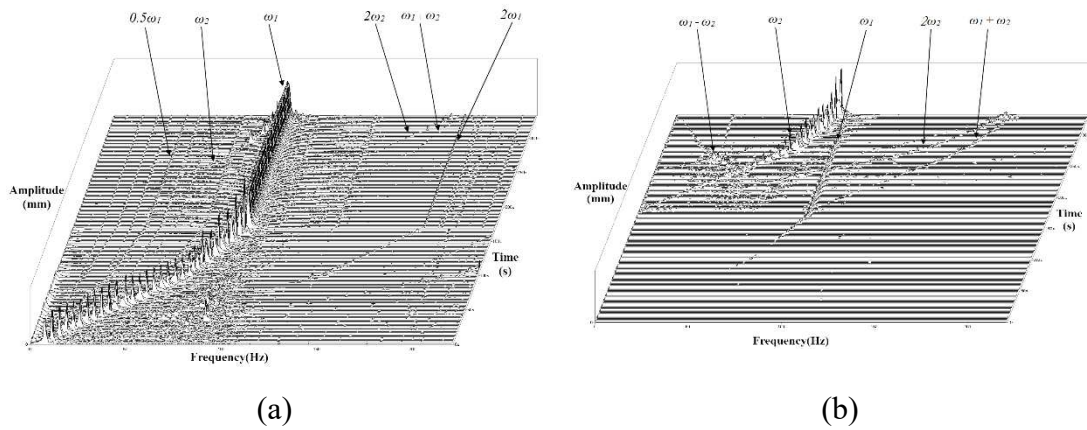


Fig. 4 Test results: measuring points for (a) gas generator (GG) rotor and (b) power turbine (PT) rotor

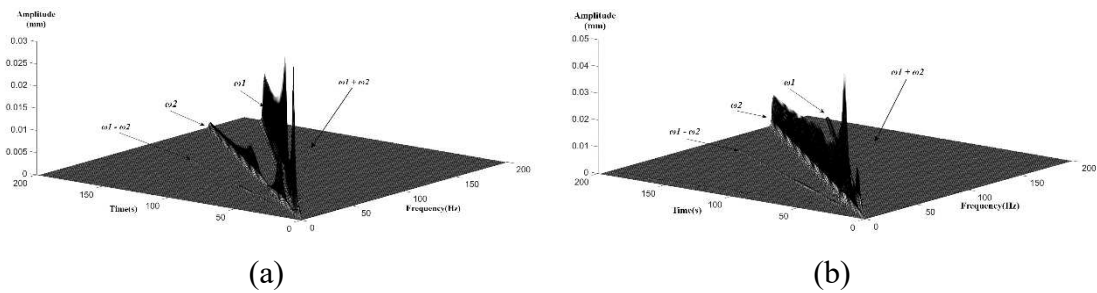


Fig. 5 Simulation analysis results: measuring points for (a) GG rotor and (b) PT rotor

4 Coupling vibration analysis of rotor-bearing system

Based on the validated analysis model in Sect. 3.4, we subject the turbine-SSS dual-rotor system to coupling vibration research. The parameters studied in this section are the imbalance of the PT rotor, the radial and bending stiffnesses of the SSS

(k_{xx} and k_{xz}), and the radial clearances of SFDs 4 and 6. We also analyze the regular influence patterns of each parameter on the amplitudes of the four frequency components of ω_1 , ω_2 , $\omega_1-\omega_2$, and $\omega_1+\omega_2$.

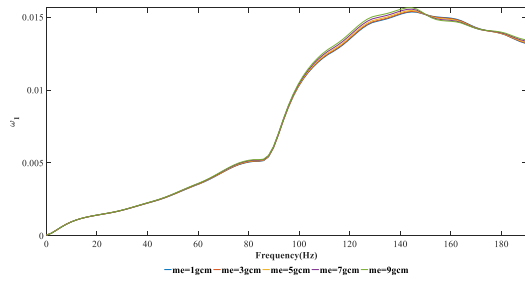
4.1 Influence of imbalance of power-turbine rotor

The imbalance of the PT rotor is given in Table 5, and the other calculation parameters of the dynamic analysis model are consistent with those of the model in Sect. 3.3. The responses at the measuring point of the PT rotor of the SSS dual-rotor system are shown in Fig. 6 for different values of the PT imbalance; Fig. 6a–d show the responses of ω_1 , ω_2 , $\omega_1-\omega_2$, and $\omega_1+\omega_2$, respectively. The responses at the measuring point of the GG rotor of the SSS rotor-bearing system are shown in Fig. 7; Fig. 7a–d show the responses of ω_1 , ω_2 , $\omega_1-\omega_2$, and $\omega_1+\omega_2$, respectively.

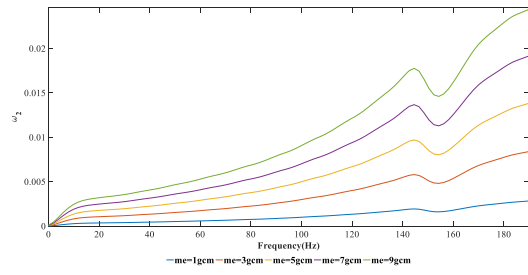
Table 5 Imbalance of PT rotor

Model	1	2	3	4	5
Imbalance [g·cm]	1	3	5	7	9

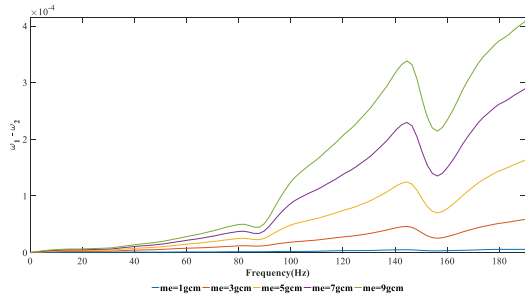
Figures 6 and 7 show that the imbalance of the PT rotor has little influence on the amplitude corresponding to ω_1 at the measuring points of the PT and GG rotors but a greater influence on the responses corresponding to ω_2 , $\omega_1-\omega_2$, and $\omega_1+\omega_2$. The responses corresponding to the latter three frequency components all increase with increasing imbalance of the PT rotor. When the imbalance of the PT rotor is small, the responses corresponding to $\omega_1-\omega_2$, and $\omega_1+\omega_2$ are extremely small and almost negligible. Therefore, we reason that exerting strict control over the spool imbalance is an effective way to control the coupling vibration response of the SSS rotor-bearing system.



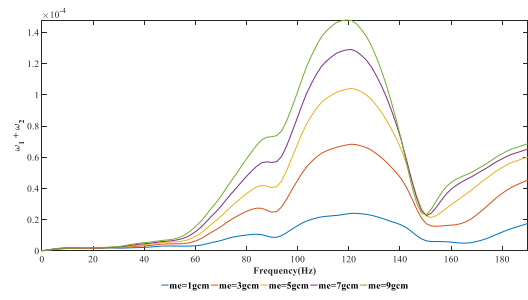
(a)



(b)

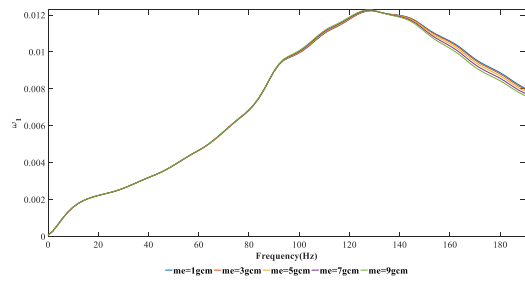


(c)

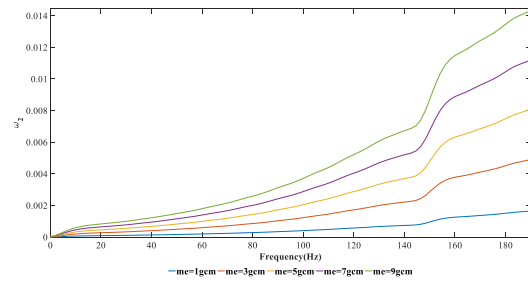


(d)

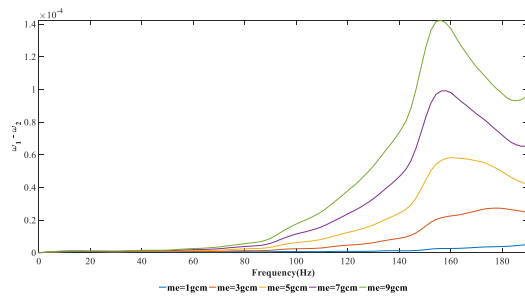
Fig. 6 Responses at measuring point of PT rotor with influence of PT rotor imbalance: (a) ω_1 ; (b) ω_2 ; (c) $\omega_1-\omega_2$; (d) $\omega_1+\omega_2$



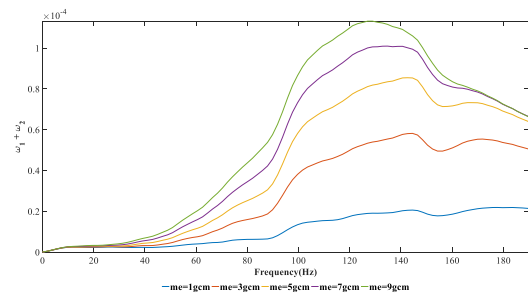
(a)



(b)



(c)



(d)

Fig. 7 Responses at measuring point of GG rotor with influence of PT rotor unbalance: (a) ω_1 ; (b) ω_2 ; (c) $\omega_1-\omega_2$; (d) $\omega_1+\omega_2$

4.2 Influence of radial stiffness of shared support structure

The radial stiffness of the SSS is given in Table 6, and the other calculation parameters of the dynamic analysis model are consistent with those of the model in Sect. 3.3.

Table 6 Radial stiffness of shared support structure (SSS)

Model	1	2	3	4	5
k_{xx} [N/m]	5×10^6	1×10^7	5×10^7	1×10^8	5×10^8

Figures 8 and 9 show the responses of the SSS rotor-bearing system at the measuring points of the PT and GG rotors, respectively, for different values of the SSS radial stiffness. Figures 8 and 9 show that with increasing SSS radial stiffness, the responses of ω_1 , $\omega_1 - \omega_2$, and $\omega_1 + \omega_2$ at the measuring points of both rotors all increase initially and then decrease. Figures 8b and 9b show that when the SSS radial stiffness is less than 1×10^7 N/m, the vibration signal of the GG rotor can hardly be observed at the measuring points of both rotors.

Combining the information in Figs. 8 and 9 shows that for a rotor-bearing system with an SSS, the probability of coupling vibration arising is reduced by avoiding certain specific values of the radial stiffness. Taking the present model as an example, from the perspective of reducing the coupling vibration response, the SSS radial stiffness should not be close to 5×10^7 N/m.

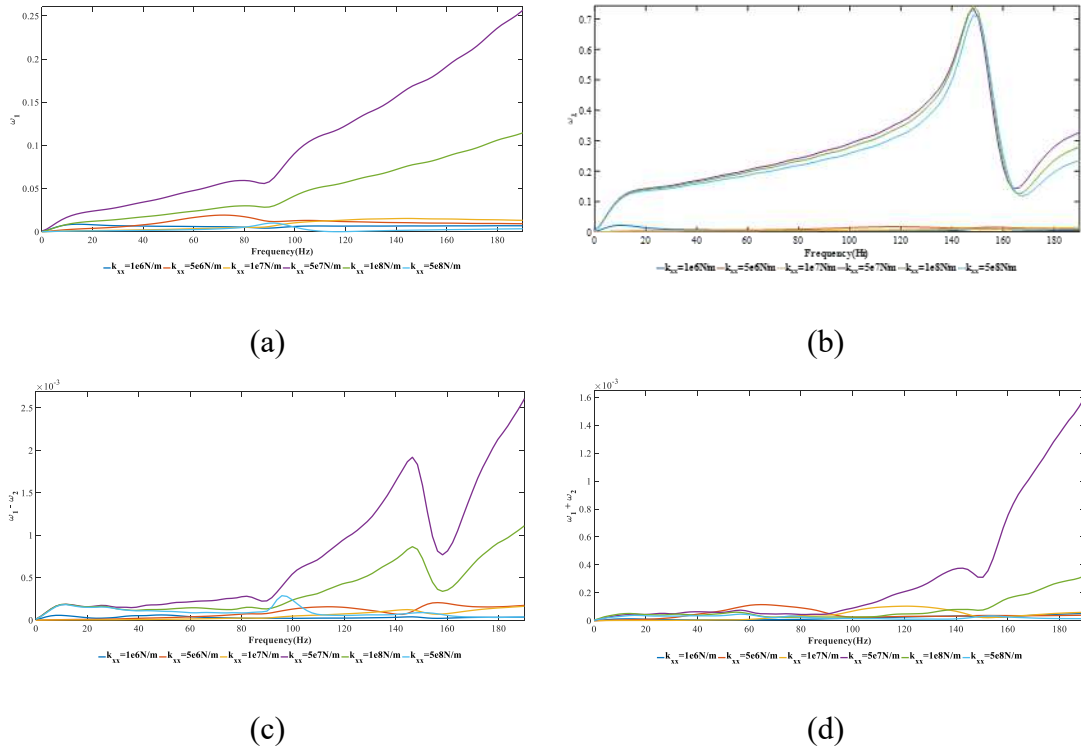


Fig. 8 Responses at measuring point of PT rotor with influence of radial stiffness of SSS: (a) ω_1 ; (b) ω_2 ; (c) $\omega_1 - \omega_2$; (d) $\omega_1 + \omega_2$

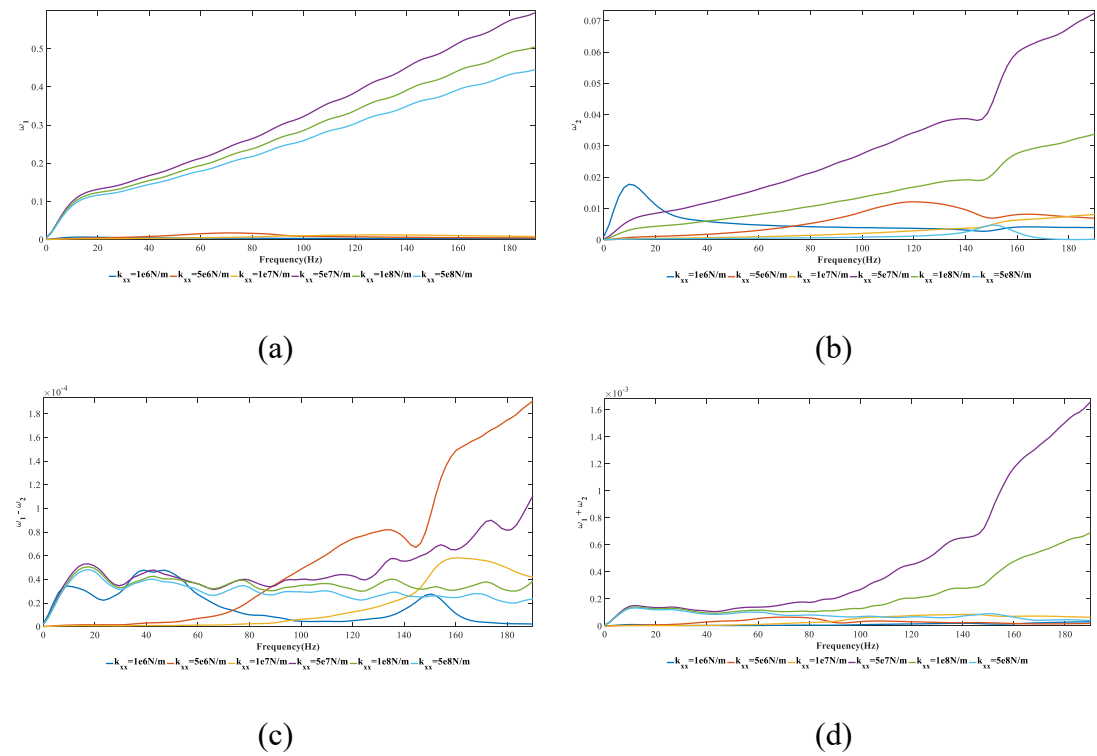


Fig. 9 Responses at measuring point of GG rotor with influence of radial stiffness of SSS: (a) ω_1 ; (b) ω_2 ; (c) $\omega_1 - \omega_2$; (d) $\omega_1 + \omega_2$

4.3 Influence of bending stiffness of shared support structure

The bending stiffness of the SSS is given in Table 7, and the other calculation parameters of the dynamic analysis model are consistent with those of the model in Sect. 3.3. Figures 10 and 11 show the responses of the SSS rotor-bearing system at the measuring points of the PT and GG rotors, respectively, for different values of the SSS bending stiffness.

Table 7 Bending stiffness of SSS

Model	1	2	3	4	5
k_{xz} [N/m]	1×10^4	1×10^5	1×10^6	1×10^7	1×10^8

Figures 10 and 11 show that when the SSS bending stiffness exceeds 1×10^6 N/m, the curves almost overlap, and the responses of frequencies ω_2 , $\omega_1 - \omega_2$, and $\omega_1 + \omega_2$ are small at the measuring points of both the PT and GG rotors. Also, when the SSS bending stiffness is low, the responses of ω_1 , ω_2 , and $\omega_1 - \omega_2$ have additional peaks in the low-frequency range. For the present SSS rotor-bearing system, when the SSS bending stiffness exceeds 1×10^6 N/m, the response of the rotor-bearing system no longer changes with changes in the SSS bending stiffness. Therefore, optimizing the SSS to have greater bending stiffness would help to suppress the low-frequency coupling vibration response of the rotor-bearing system and reduce the ω_2 response.

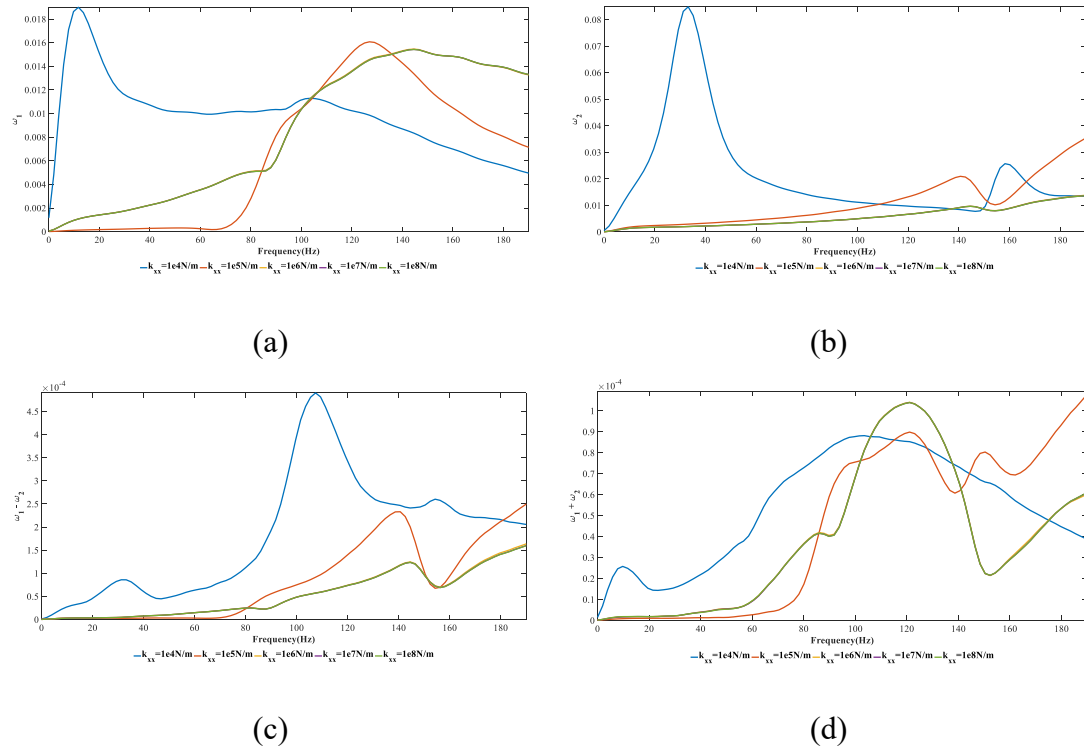


Fig. 10 Responses at measuring point of PT rotor with influence of bending stiffness of SSS: (a) ω_1 ; (b) ω_2 ; (c) $\omega_1 - \omega_2$; (d) $\omega_1 + \omega_2$

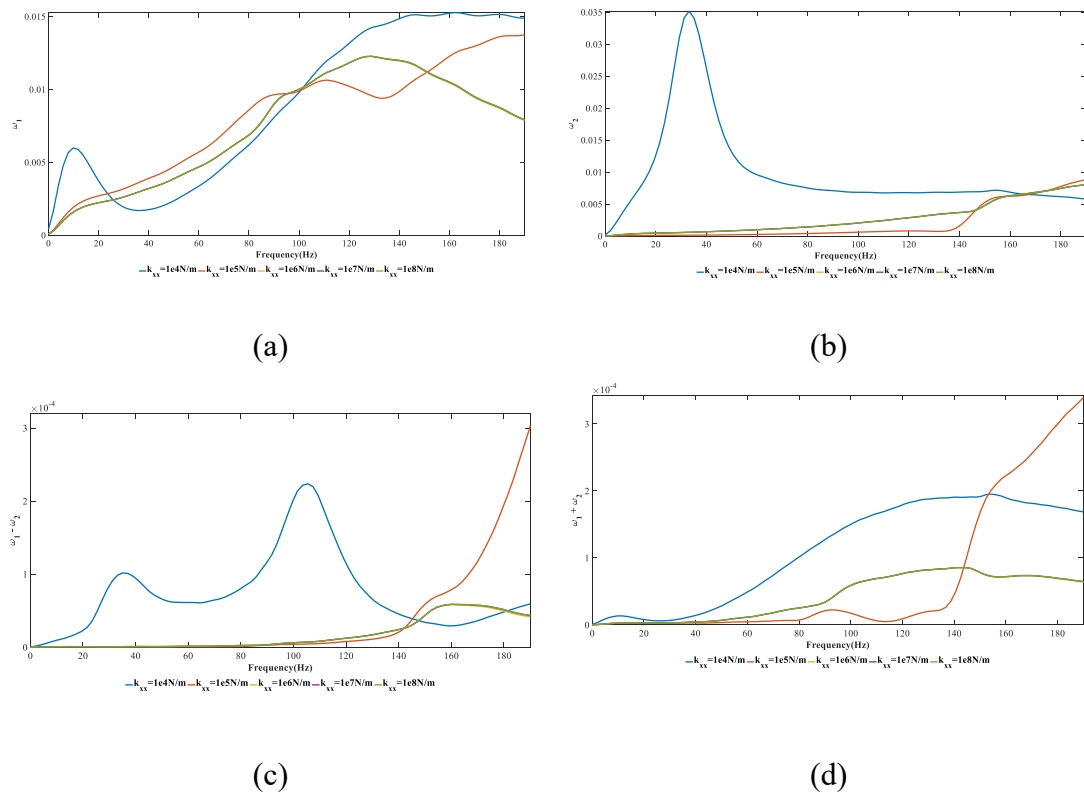


Fig. 11 Responses at measuring point of GG rotor with influence of bending stiffness of SSS: (a) ω_1 ; (b) ω_2 ; (c) $\omega_1 - \omega_2$; (d) $\omega_1 + \omega_2$

4.4 Influence of radius clearance of SFD 4

The radius clearance of SFD 4 is given in Table 8 and corresponds to 1–3‰ of the journal radius. The other calculation parameters of the dynamic analysis model are consistent with those of the model in Sect. 3.3. Figures 12 and 13 show the response of the SSS rotor-bearing system at the measuring points of the PT and GG rotors, respectively, for different values of the radius clearance of SFD 4.

Table 8 Radius clearance of SFD 4

Model	1 (1‰)	2 (1.5‰)	3 (2‰)	4 (2.5‰)	5 (3‰)
Radius clearance [mm]	0.031	0.046	0.061	0.076	0.092

Figure 12a–c show that the responses of ω_1 , ω_2 , and $\omega_1-\omega_2$ at the measuring point of the PT rotor all decrease with increasing radius clearance of SFD 4. Before 140 Hz, the response of $\omega_1+\omega_2$ at the measuring point of the PT rotor decreases with increasing radius clearance, and the peak response decreases by more than 50%. After 140 Hz, the response of $\omega_1+\omega_2$ for each radius gap is at a low level. Figure 13b and d show that the responses of ω_2 and $\omega_1+\omega_2$ at the measuring point of the GG rotor decrease with increasing radius clearance of SFD 4. The response of $\omega_1-\omega_2$ at the measuring point of the GG rotor decreases with increasing radius clearance before 140 Hz; after 140 Hz, the response of $\omega_1-\omega_2$ does not change regularly with the radius clearance of SFD 4, but in general the peak response for large radius clearance is smaller than that for small radius clearance. As radius clearance of SFD 4 increases, the response of ω_1 at the measuring point of the GG rotor increases before 90 Hz, and then reduces after 90 Hz, but judging from the response amplitude, the response amplitude for large oil-film thickness has a smaller range of change and the maximum amplitude in the full frequency range is smaller than the response amplitude for small radius clearance of SFD 4.

Therefore, increasing the oil-film clearance of SFD 4 within a reasonable range would help to (i) suppress the coupling vibration response of the SSS rotor-bearing system and (ii) reduce the responses corresponding to the fundamental frequencies of the PT and GG rotors.

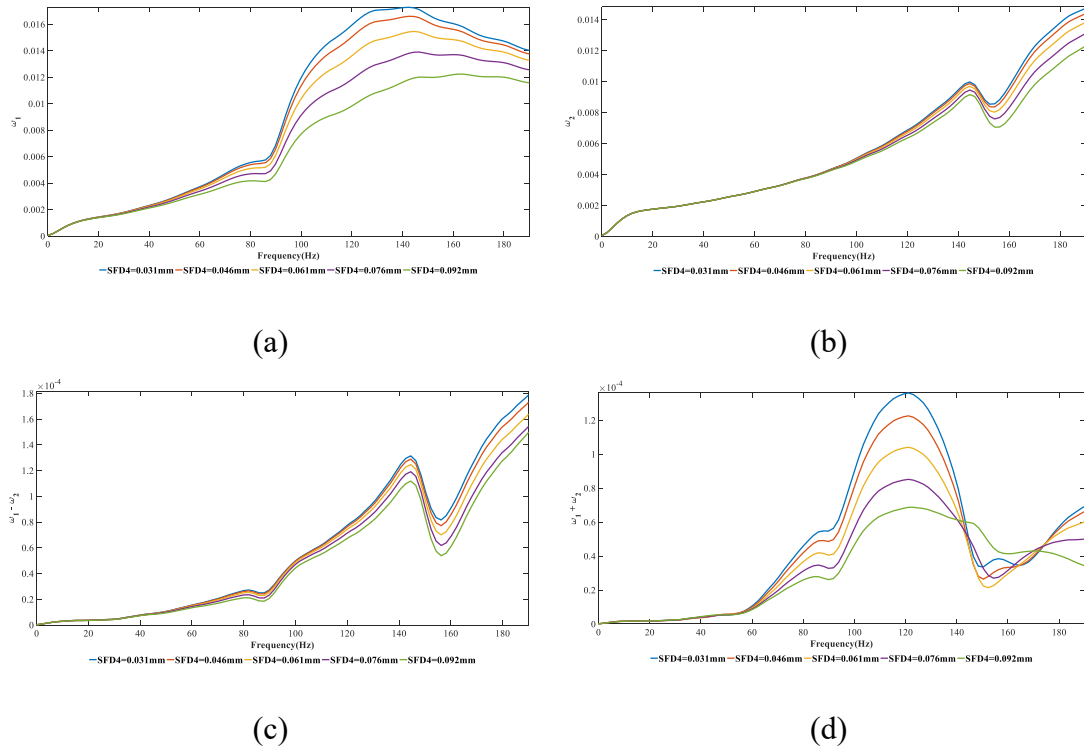


Fig. 12 Responses at measuring point of PT rotor with influence of radius clearance of SFD 4: (a) ω_1 ; (b) ω_2 ; (c) $\omega_1 - \omega_2$; (d) $\omega_1 + \omega_2$

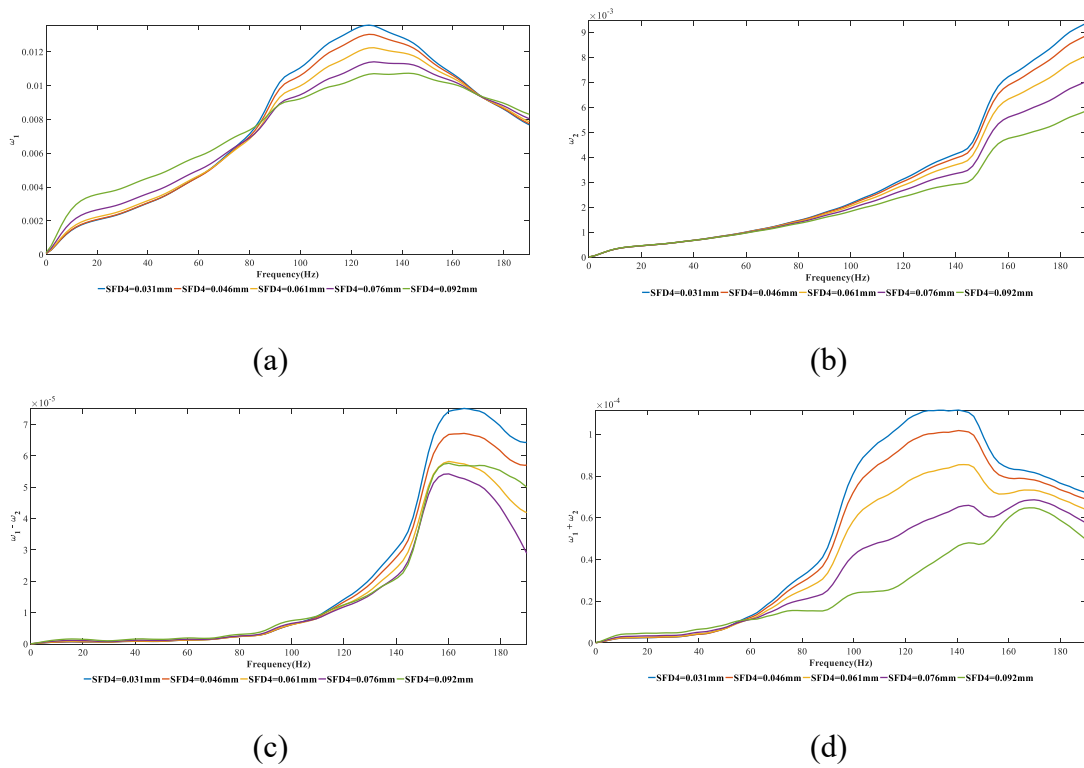


Fig. 13 Responses at measuring point of GG rotor with influence of radius clearance of SFD 4: (a) ω_1 ; (b) ω_2 ; (c) $\omega_1 - \omega_2$; (d) $\omega_1 + \omega_2$

4.5 Influence of radius clearance of SFD 6

The radius clearance of SFD 6 is given in Table 9 and corresponds to 1–3‰ of the journal radius. The other calculation parameters of the dynamic analysis model are consistent with those of the model in Sect. 3.3. Figures 14 and 15 show the responses of the SSS rotor-bearing system for different values of the radius clearance of SFD 6.

Table 9 Radius clearance of SFD 6

Model	1 (1‰)	2 (1.5‰)	3 (2‰)	4 (2.5‰)	5 (3‰)
Radius clearance [mm]	0.027	0.040	0.061	0.053	0.080

Comparing the response amplitudes of each frequency in Figs. 14 and 15 shows that the oil-film thickness of SFD 6 has a greater impact on the response amplitudes of frequencies ω_1 and $\omega_1 - \omega_2$ at the measuring points of both the PT and GG rotors but little influence on those of ω_2 and $\omega_1 + \omega_2$. From the perspective of suppressing the maximum amplitude, a reasonable increase in the oil-film clearance of SFD 6 would help to reduce the response amplitudes of ω_1 and $\omega_1 - \omega_2$ at the measuring points of the PT and GG rotors of the SSS rotor-bearing system.

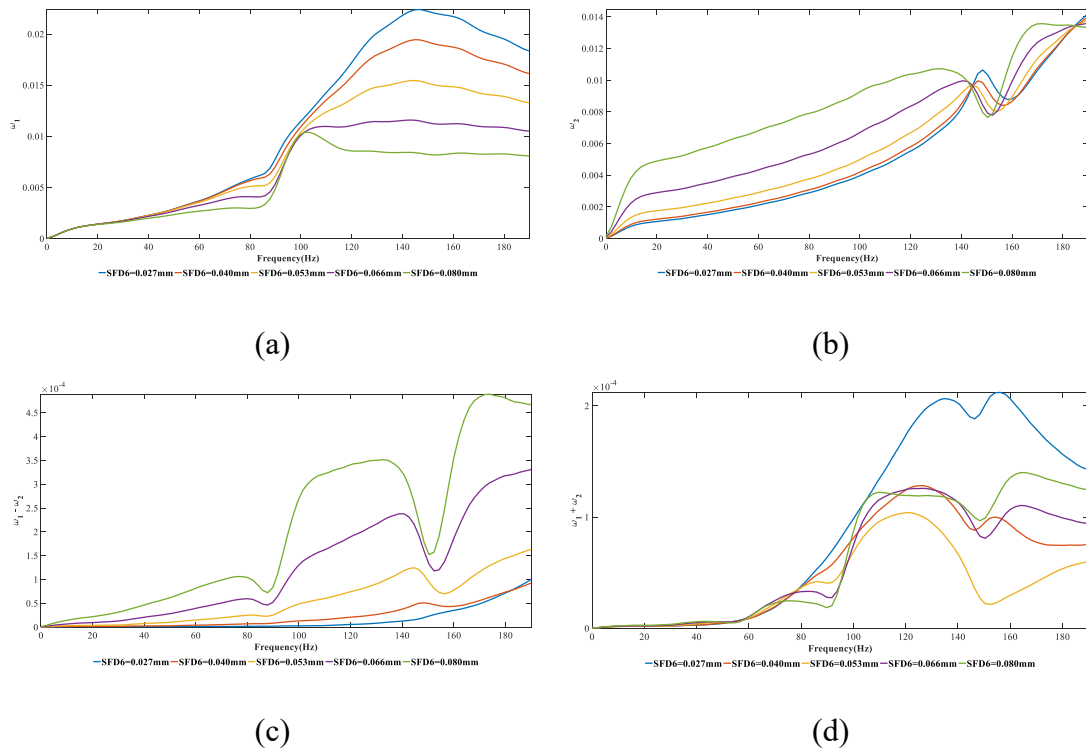


Fig. 14 Responses at measuring point of PT rotor with influence of radius clearance of SFD 6: (a) ω_1 ; (b) ω_2 ; (c) $\omega_1 - \omega_2$; (d) $\omega_1 + \omega_2$

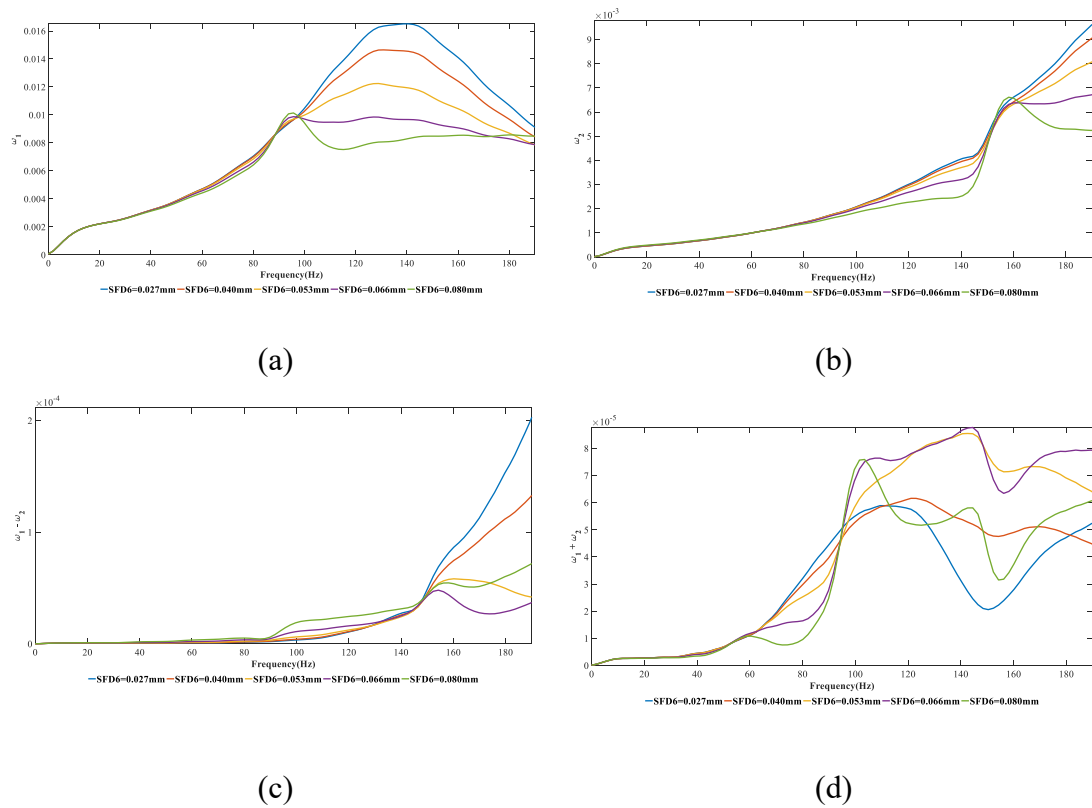


Fig. 15 Responses at measuring point of GG rotor with influence of radius clearance of SFD 6: (a) ω_1 ; (b) ω_2 ; (c) $\omega_1 - \omega_2$; (d) $\omega_1 + \omega_2$

5 Conclusions

Based on the features of a turboshaft engine with a turbine SSS, a test system with a turbine SSS was designed, and an FE model of the test system was established. We studied how the imbalance of the PT rotor, the radial and bending stiffnesses of the SSS, and the radius clearances of the SFDs at the SSS affected the coupling vibration response of the rotor-bearing system, and the main conclusions are as follows.

Both the experimental and theoretical research showed that an SSS rotor-bearing system with SFDs may exhibit coupling vibration responses with frequencies $\omega_1 - \omega_2$ and $\omega_1 + \omega_2$.

The experimental verification showed that the dynamic analysis model of the rotor-bearing system with an SSS established by FE modeling is accurate and reliable. Theoretical research using this dynamic analysis model can better reflect the coupling vibration of a rotor-bearing system with an SSS.

The spool imbalance in an aeroengine has a greater impact on the coupling vibration response of a rotor-bearing system with an SSS. Exerting strict control over

the spool imbalance would help to suppress the coupling vibration response of a rotor-bearing system with an SSS.

The SSS radial stiffness (k_{xx}) should avoid certain specific frequency components to reduce the probability of coupling vibration arising in an SSS rotor-bearing system. Furthermore, a larger SSS bending stiffness (k_{xz}) has a positive impact on suppressing the coupling vibration response of a rotor-bearing system with an SSS.

Finally, in a reasonable range, increasing the radial clearances of the SFDs at the SSS would help to reduce the response amplitude of a rotor-bearing system with an SSS.

Acknowledgments This work was supported by the National Natural Science Foundation of China (Grant Ref. 51775266) and the National Major Science and Technology Projects of China (Grant Ref. 2017-IV-0006-0043).

Compliance with ethical standards

Conflict of interest The authors declare that they have no conflict of interest.

References

- [1] Seda, J.F.: Aircraft engine with inter-turbine engine frame. US Patent US6708482 (2005)
- [2] Kumar, K.B., Somanath, N., Sowa, W.A.: Mid-turbine frame. US Patent US8181466 (2012)
- [3] Lu, K., Chen, Y., Cao, Q., Hou, L., Jin, Y.: Bifurcation analysis of reduced rotor model based on nonlinear transient POD method. *Int. J. Non-Linear Mech.* **89**, 83–92 (2017)
- [4] Lu, K., Yang, Y., Xia, Y., Fu, C.: Statistical moment analysis of nonlinear rotor system with multi uncertain variables. *Mech. Syst. Signal Process.* **116**, 1029–1041 (2018)
- [5] Thiery, F., Aidanpää, J.O.: Nonlinear vibrations of a misaligned bladed Jeffcott rotor. *Nonlinear Dyn.* **86**, 1807–1821 (2016)
- [6] Yang, R., Jin, Y., Hou, L., Chen, Y.: Study for ball bearing outer race characteristic defect frequency based on nonlinear dynamics analysis. *Nonlinear Dyn.* **90**, 781–796 (2017)

- [7] Gao, P., Hou, L., Yang, R., Chen, Y.: Local defect modeling and nonlinear dynamic analysis for the inter-shaft bearing in a dual-rotor system. *Appl. Math. Model.* **68**, 29–47 (2019)
- [8] Gao, P., Chen, Y., Hou, L.: Nonlinear thermal behaviors of the inter-shaft bearing in a dual-rotor system subjected to the dynamic load. *Nonlinear Dyn.* **101**, 191–209 (2020)
- [9] Hou, L., Chen, Y., Fu, Y., Chen, H., Lu, Z., Liu, Z.: Application of the HB–AFT method to the primary resonance analysis of a dual-rotor system. *Nonlinear Dyn.* **88**, 2531–2551 (2017)
- [10] Lu, K., Jin, Y., Huang, P., Zhang, F., Zhang, H., Fu C., Chen, Y.: The applications of POD method in dual rotor-bearing systems with coupling misalignment. *Mech. Syst. Signal Process.* (2021). <https://doi.org/10.1016/j.ymssp.2020.107236>
- [11] Wang, N., Liu, C., Jiang, D., Behdinan, K.: Casing vibration response prediction of dual-rotor-blade-casing system with blade-casing rubbing. *Mech. Syst. Signal Process.* **118**, 61–77 (2019)
- [12] Chen, G.: Simulation of casing vibration resulting from blade–casing rubbing and its verifications. *J. Sound Vib.* **361**, 190–209 (2016)
- [13] Yu, P., Zhang, D., Ma, Y., Hong, J.: Dynamic modeling and vibration characteristics analysis of the aero-engine dual-rotor system with fan blade out. *Mech. Syst. Signal Process.* **106**, 158–175 (2018)
- [14] Yang, Y., Ouyang, H., Yang, Y., Cao, D., Wang, K.: Vibration analysis of a dual-rotor-bearing-double casing system with pedestal looseness and multi-stage turbine blade-casing rub. *Mech. Syst. Signal Process.* (2020). <https://doi.org/10.1016/j.ymssp.2020.106845>
- [15] Nelson, H.D., McVaugh, J.M.: The dynamics of rotor-bearing systems using finite elements. *J. Eng. Ind. ASME* **98**, 593–600 (1976)
- [16] Nelson, H.D.: A finite rotating shaft element using Timoshenko beam theory. *J. Mech. Des. ASME* **102**, 793–803 (1980)
- [17] Glasgow, D.A., Nelson, H.D.: Stability analysis of rotor-bearing systems using component mode synthesis. *J. Mech. Des. ASME* **102**, 352–359 (1980)
- [18] Nelson, H.D., Meacham, W.L., Fleming, D.P., Kascak, A.F.: Nonlinear analysis of rotor-bearing systems using component mode synthesis. *J. Mech. Des. ASME* **105**, 606–614 (1983)
- [19] Chiang, H.D., Hsu, C., Jeng, W., Tu, S. Li, W.: Turbomachinery dual

- rotor-bearing system analysis. *ASME Turbo Expo: Power for Land, Sea, and Air* **36096**, 803–810 (2002)
- [20]Chiang, H.D., Hsu, C., Tu, S.: Rotor-bearing analysis for turbomachinery single-and dual-rotor systems. *J. Propuls. Power* **20**, 1096–1104 (2004)
- [21]Wang, F., Luo, G., Yang, X., Cui, H.: Research on modeling and dynamic characteristics of complex coaxial rotor system. *J. Vibroeng.* **19**, 1524–1545 (2017)
- [22]Della Pietra, L., Adiletta, G.: The squeeze film damper over four decades of investigations. Part I: Characteristics and operating features. *Shock Vib. Digest.* **34**, 3–26 (2002)
- [23]Adiletta, G., Della Pietra, L.: The squeeze film damper over four decades of investigations. Part II: Rotordynamic analyses with rigid and flexible rotors. *Shock Vib. Digest.* **34**, 97–126 (2002)
- [24]Heidari, H.R., Safarpour, P.: Design and modeling of a novel active squeeze film damper. *Mech. Mach. Theory* **105**, 235–243 (2016)
- [25]Groves, K.H., Bonello, P.: Improved identification of squeeze-film damper models for aeroengine vibration analysis. *Tribol. Int.* **43**, 1639–1649 (2010)
- [26]Rezvani, M.A., Hahn, E.J.: Floating ring squeeze film damper: theoretical analysis. *Tribol. Int.* **33**, 249–258 (2000)
- [27]San Andres, L.: Force coefficients for a large clearance open ends squeeze film damper with a central feed groove: experiments and predictions. *Tribol. Int.* **71**, 17–25 (2014)
- [28]Zhao, M., Ren, P.Z., Li, J.Q., Yang, H.Y., Liu, J.Y.: Double static analysis of muti-rotor system with squeeze film damper. *J. Propuls. Technol.* **25**(1), 66–70 (2004) (in Chinese)
- [29]Inayat-Hussain, J.I., Kanki, H., Mureithi, N.W.: Chaos in the unbalance response of a rigid rotor in cavitated squeeze-film dampers without centering springs. *Chaos Solitons Fractals* **13**, 929–945 (2002)
- [30]Qin, W., Zhang, J., Ren, X.: Response and bifurcation of rotor with squeeze film damper on elastic support. *Chaos Solitons Fractals* **39**, 188–195 (2009)
- [31]Chen, H., Hou, L., Chen, Y.: Bifurcation analysis of a rigid-rotor squeeze film damper system with unsymmetrical stiffness supports. *Arch. Appl. Mech.* **87**, 1347–1364 (2017)
- [32]Luo, Z., Wang, J., Tang, R., Wang, D.: Research on vibration performance of the

nonlinear combined support-flexible rotor system. *Nonlinear Dyn.* **98**, 113–128 (2019)

[33] Inayat-Hussain, J.I.: Bifurcations in the response of a flexible rotor in squeeze-film dampers with retainer springs. *Chaos Solitons Fractals* **39**, 519–532 (2009)